Postplasma Catalytic Model for NO Production: Revealing the Underlying Mechanisms to Improve the Process Efficiency

Hamid Ahmadi Eshtehardi,* Kevin Van 't Veer, Marie-Paule Delplancke, Francois Reniers, and Annemie Bogaerts*

ACCESS | Metrics & More | Article Recommendations | Supporting Information

ABSTRACT: Plasma catalysis is emerging for plasma-assisted gas conversion processes. However, the underlying mechanisms of plasma catalysis are poorly understood. In this work, we present a 1D heterogeneous catalysis model with axial dispersion (i.e., accounting for back-mixing and molecular diffusion of fluid elements in the process stream in the axial direction), for plasma-catalytic NO production from N_2/O_2 mixtures. We investigate the concentration and reaction rates of each species formed as a function of time and position across the catalyst, in order to determine the underlying mechanisms. To obtain insights into how the performance of the process can be further improved, we also study how changes in the postplasma gas flow composition entering the catalyst bed and in the operation conditions of the catalytic stage affect the performance of NO production.

KEYWORDS: N_2 fixation, plasma catalysis, heterogeneous catalysis, nonthermal plasma, axial dispersion model, plasma reactor
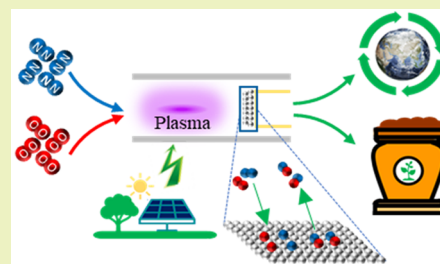
INTRODUCTION

Plasma technology is gaining increasing interest for nitrogen fixation into either NH_3 or NO_x.[1,2] The reason is that in nonthermal plasmas (NTPs), the electrons have a temperature of thousands of degrees, while the bulk gas is close to room temperature.[3] Hence, the electrons can activate the gas molecules, by (vibrational and electronic) excitation, ionization, and dissociation, which is more cost-efficient than just thermal dissociation. However, due to the high reactivity of NTP, it is difficult to selectively produce the desired products. Hence, NTP is combined with catalysts in so-called plasma catalysis to improve the reaction selectivity.[4]

One of the earliest reports on plasma catalysis is a U.S. patent by Henis for NO_x removal.[5] On the other hand, Rapakoulias et al. studied the NO_x synthesis in an inductively coupled high frequency plasma reactor using MoO_3 and WO_3 as a catalyst. The NO_x yield reported was 8% without catalyst, and increased to 19% by using the WO_3 catalyst.[6] MoO_3 was also coated on the reactor wall of a microwave plasma by Mutel et al.[7] An energy cost of 0.93 MJ/mol-N was reported for NO production, which provided 78% improvement in energy efficiency compared to the plasma process without catalyst. Sun et al. studied the NO_x formation in a dielectric barrier discharge (DBD) reactor with single stage configuration using CuZSM-5 as a catalyst. Temperatures above 350 °C were favorable for NO_x production.[8] Plasma-catalytic NO production in a glow discharge reactor was investigated by Belova and Eremin, who found the catalyst effectiveness to be on the order of Pt > CuO > Cu > Fe > Ag.[9,10]

Modeling of plasma-catalytic NO production can be useful to better understand the mechanisms and tune the process. Ideal reactor models, such as the continuously stirred tank reactor (CSTR) and plug flow reactor (PFR) models, are based on idealized assumptions (i.e., perfect mixing and no back-mixing, respectively).[11] Of course, these simplified assumptions do not reflect reality, as real reactors exhibit some degree of back-mixing. Tanks-in-series models (TISM) and axial dispersion models (ADM), on the other hand, are one-parameter models that describe reactors that are partially mixed.[12] Recently, Ma et al. employed a CSTR model, in combination with experiments, to study plasma-catalytic NO production in a radio frequency inductively coupled plasma (ICP) reactor at low pressure using a Pt catalyst. They investigated the synergistic effect of plasma and postdischarge catalysts on the production of NO, and determined the major NO production mechanisms.[13]

ADMs, which account for back-mixing and molecular diffusion in the axial direction, are very robust for modeling fixed bed catalytic reactors and have been widely used for investigation of various catalytic processes.[14−22] In the present work, for the first time, we developed such a model for postplasma catalytic production of NO. Compared to CSTR
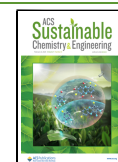
models, as studied by Ma et al.,[13] this modeling approach is more complicated. However, it provides more information, as it allows one to determine the concentration of all species as a function of both time and position across the catalyst bed (in the axial direction), both in the gas phase and on the catalyst surface. Additionally, it allows one to study the reactor and catalyst bed design, as well as the effect of operation conditions, toward process optimization.

The aim of our paper is to introduce this ADM approach for modeling of a plasma-catalytic process, which can provide useful insights in how, when, and where different mechanisms play a role, in favor of, or against the pathways toward the desired product, i.e., NO. In first instance, we apply our model to the experiments of Ma et al.[13] However, as the exact concentrations of different species (except for NO) in the postplasma gas that enters the catalyst bed were not available in their study, we first check the NO production sensitivity to these concentrations, to estimate the ranges in which our model can reproduce the experimental results and also to obtain more insight into how the postplasma gas composition can affect the reaction performance in the catalytic bed. Additionally, we will investigate the effect of the degree of back-mixing on the outlet concentration of NO, in a wide range from close to a PFR to close to a CSTR. Finally, we will study the effect of the catalyst bed characteristic length and porosity on the system performance, and we will discuss the mechanisms behind the observed effects. Our model presented here is applied to plasma-catalytic NO production, but the concept will be more generally valid for other plasma-catalytic systems as well.

■ MODEL DESCRIPTION

Dispersion Model: Adverse Effect of Back-Mixing. Our 1D heterogeneous catalysis dispersion model accounts for mass transfer in the gas and solid phase, as well as the energy and momentum balances across the catalyst bed. In general, the term dispersion (back-mixing) is used to denote the combined action of all phenomena (i.e., diffusion and nonuniform velocities), which give rise to a certain distribution of residence times in a reactor (i.e., not the same residence time for all gas molecules, like in a PFR or CSTR). Back-mixing is the tendency of reacted species to intermingle with unreacted feed gas in a reactor, which affects the performance of a chemical reactor in terms of conversion, product yields, and selectivity. Back-mixing in a flow reactor has a definite adverse effect on the performance of the process. Additionally, the higher the reaction order, the higher the adverse effect of the back-mixing.[23] PFR and CSTR models are ideal reactor models that are conventionally used to describe flow reactors. In a PFR model, no mixing in the axial (i.e., flow) direction is assumed, while a CSTR model assumes perfect mixing.[11] However, real flow reactors always exhibit a degree of back-mixing. Hence, PFR and CSTR models cannot predict the true performance of a real flow reactor.[12,23] The degree of back-mixing is represented by the Peclet (Pe) number (Pe = $u_s L / D_z$), where u_s, L, and D_z stand for gas superficial velocity, catalyst bed characteristic length, and axial dispersion coefficient, respectively. In a PFR, Pe → ∞ (i.e., $D_z = 0$), and in a CSTR, Pe = 0 (i.e., $D_z → ∞$). In real reactors, the degree of back-mixing is in between those of a PFR and CSTR.

When considering a fluid in plug flow, with some degree of back-mixing, independent of the position within the reactor, it implies that no stagnant regions or gross bypassing of the fluid exist in the reactor. This is called the dispersed plug flow model or simply dispersion model. Since the mixing process involves redistribution of material either by slippage or eddies, and since this is repeated many times during the fluid flow through the reactor, we can consider these disturbances to be statistic in nature, somewhat as in molecular diffusion. For molecular diffusion, Fick's second law predicts how diffusion causes the concentration of a substance to change with respect to time, and the diffusion coefficient uniquely characterizes this diffusion process. In an analogous manner, one may consider all the contributions to intermixing and molecular diffusion of a fluid flowing in the axial direction to be described by an axial dispersion coefficient. The term axial is used to distinguish mixing in the direction of the flow from mixing in the lateral direction.[11] Of course, in any tubular reactor, either empty or packed, reactant depletion and nonuniform flow velocity profiles give rise to concentration gradients, and hence diffusion, in both axial and lateral directions. In addition, in turbulent flow, eddy transport takes place, tending to level out gradients in all directions to an even greater extent than does molecular diffusion. Developing a reactor model which accurately reflects these phenomena is very challenging. Therefore, some assumptions are typically made, as explained in next section.

Model Assumptions. We made the following assumptions to derive the governing mathematical equations:

(a) An ideal PFR has a fixed residence time, meaning that any fluid (plug) that enters the reactor at time t will exit the reactor at time $t + \tau$, where τ is the residence time of the fluid in the reactor. The residence time distribution function for an ideal PFR is therefore a Dirac delta function at τ. A real PFR, on the other hand, has a residence time distribution that is a narrow pulse around the mean residence time distribution. As explained in previous section, ideal PFR models cannot be applied for a real reactor, so dispersion models are usually employed.[24,25] Our dispersion model assumes that the reactor is in plug flow (but not ideal plug flow): the gas composition and temperature are radially uniform, and the process fluid moves through the reactor at a uniform velocity equal to the mean velocity of the fluid in the reactor.

(b) Dispersion occurs in the axial direction. The extent of dispersion is sufficient to account for the combined effects of all dispersive phenomena (molecular and turbulent mixing, and nonuniform velocities) in the real reactor. This representation of a flow reactor is termed the dispersed plug flow model or simply the axial dispersion model. As shown in the literature, these models can successfully simulate the behavior of reactors in which complex radial and axial flow and transport patterns exist.[26]

(c) Nonadiabatic processes can develop significant radial temperature gradients due to heat transfer at the wall. Temperature gradients will produce radial concentration gradients as well. Therefore, the process is assumed to be adiabatic in nature.

(d) The ideal gas law is applicable.

(e) The catalyst particles are small enough (<0.1 mm) so that no temperature gradient should be considered within the catalyst particles. Additionally, in such a case, intraporous mass and energy transport limitations can be
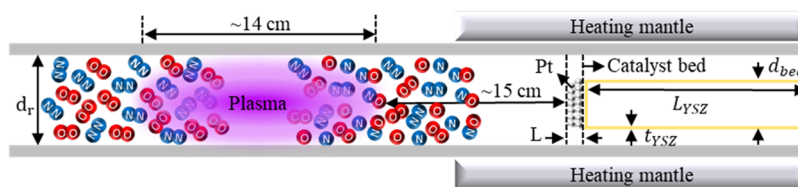
Figure 1. Schematic overview of the modeled experimental reactor setup, based on ref 13.

neglected (i.e., each point on the interior of the catalyst particle surface is accessible for each species to react); therefore, the so-called catalyst effectiveness factor, η_j, is assumed to be unity for all the reactions (see section SI.1 for more information).

(f) As the reactor under study is categorized as a fixed bed reactor, only negligible movements of the catalyst particles (due to fluid flow) occur in the catalyst bed. Therefore, the porosity of the bed is assumed to be constant.

Experimental Setup to Be Modeled. A schematic overview of the modeled experimental setup[13] is shown in Figure 1. Using an inductive coil connected to a matching network of a radio frequency (RF) generator, a plasma with a length of about 14 cm is generated. The catalyst (porous Pt film on an yttria-stabilized zirconia (YSZ) support, with 2 mm thickness (t_{YSZ} in Figure 1), 25 mm diameter (d_{bed} in Figure 1), and 245 mm length (L_{YSZ} in Figure 1)) is located at about 15 cm from the plasma. The temperature at the catalytic part of the reactor is controlled by a heating mantle, which is kept at 873 K. To perform the experiments, a mixture of N_2/O_2 at 5 mbar is injected to the reactor at a flow rate of 100 sccm. The flowing gas mixture is activated by the RF plasma source with a power of about 80 W. A quadrupole mass spectrometer is used to measure the composition of the outflowing gas mixture from the reactor. A full description of the experiments is given in ref 13. As illustrated in Figure 1, the reactor consists of 2 different stages, i.e., a plasma stage followed by a catalytic stage. In this study, we only focus on modeling the catalytic stage. Finally, the deposited Pt catalyst particles on the YSZ support are assumed as a the set of packed particles are located in a catalyst bed with a diameter identical to the diameter of the YSZ support. Therefore, the system is modeled as a packed bed reactor and radial nonuniformities are neglected.

Governing Equations. The governing equations can be derived from the mass, energy and momentum balances on a slice of infinitesimal thickness dz (as depicted in Figure 2) during an infinitesimal time dt.[21,22]

In the following, we describe the mass and energy balance in the gas and solid phase in the catalytic bed, respectively, as well
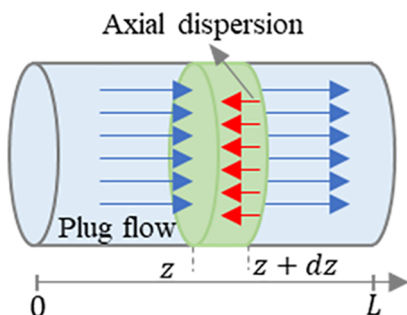
as the Ergun equation for the pressure drop across the catalyst bed, which accounts for the momentum transfer.

Mass and Energy Balance in the Gas Phase (Equations 1 and 2).

$$\varepsilon_b\left(\frac{\partial C_i}{\partial t}\right) + u_s\frac{\partial C_i}{\partial z} + k_{g,i}a_v(C_i - C_{i,s}) = \varepsilon_b D_z\frac{\partial^2 C_i}{\partial z^2} + r_i^{gas} \tag{1}$$

In eq 1, the term $\varepsilon_b\frac{\partial C_i}{\partial t}$ represents the transient behavior of the concentration, C_i, of species i in the gas phase, where ε_b is the catalyst bed porosity. The term $u_s\frac{\partial C_i}{\partial z}$ accounts for changes in the concentration of gas phase species i in the axial direction due to convection, where u_s is the superficial gas velocity. The term $k_{g,i}a_v(C_i - C_{i,s})$ represents the mass transfer of species i from the gas phase to the solid phase (catalyst surface), where $k_{g,i}$ is the gas-to-solid mass transfer coefficient of component i and a_v is the external surface area per unit volume of the catalyst bed. In other words, this term represents the adsorption of the gas phase species on the catalyst surface. Therefore, it can be replaced by the adsorption rate for each species, that is calculated based on transition state theory in the surface model (i.e., $k_{g,i}a_v(C_i - C_{i,s}) = r_{ads}$). Finally, the term $\varepsilon_b D_z\frac{\partial^2 C_i}{\partial z^2}$ stands for the changes in the concentration of species i in the gas phase due to axial dispersion, with D_z the axial dispersion coefficient. Finally, the term r_i^{gas} represents the production or destruction of species i through the gas phase reactions.

$$\varepsilon_b\rho_g C_{pg}\left(\frac{\partial T_g}{\partial t}\right) + u_s\rho_g C_{pg}\frac{\partial T_g}{\partial z} = h_f a_v(T_s - T_g) + \lambda_z^f\frac{\partial^2 T_g}{\partial z^2} \tag{2}$$

In eq 2, the term $\varepsilon_b\rho_g C_{pg}\frac{\partial T_g}{\partial t}$ accounts for the changes in the gas phase temperature, T_g, as a function of time, where ρ_g is the gas phase density and C_{pg} is the heat capacity of the gas phase. The term $u_s\rho_g C_{pg}\frac{\partial T_g}{\partial z}$ represents the gas phase temperature changes through convective heat transfer throughout the axial direction, z, due to movement of the gas phase across the catalyst bed, where u_s is the gas superficial velocity. The term $h_f a_v(T_s - T_g)$ stands for the heat transfer between the bulk of the gas and the solid phase, with h_f the heat transfer coefficient, and T_s the temperature at the catalyst surface. Finally, the term $\lambda_z^f\frac{\partial^2 T}{\partial z^2}$ denotes changes in the gas temperature through the axial direction of the catalyst bed due to conductive heat transfer, with λ_z^f the effective axial thermal conductivity.

(Mass and Energy Balance in the Solid Phase (Equations 3 and 4).

$$\frac{\partial C_{i,s}}{\partial t} - k_{g,i}a_v(C_i - C_{i,s}) = (1 - \varepsilon_b)r_i^s \tag{3}$$

Figure 2. Side view of the modeled catalytic part of the reactor setup.

In eq 3, the term $\frac{\partial C_{i,s}}{\partial t}$ represents the time-dependent change in concentration of species i on the catalyst surface (i.e., in the solid phase), and the term $(1 - \varepsilon_b)r_i^s$ accounts for the production or destruction of species i through surface reactions in the solid phase.

$$\rho_{bed}C_{p,bed}\left(\frac{\partial T_s}{\partial t}\right) + h_f a_v(T_s - T_g)$$
$$= (1 - \varepsilon_b)\sum - \Delta H_{rxn,j}\eta_j R_j \tag{4}$$

Finally, in eq 4, $\rho_{bed}C_{p,bed}\frac{\partial T_s}{\partial t}$ accounts for time-dependent temperature changes of the solid phase with ρ_{bed} and $C_{p,bed}$ the density and heat capacity of the catalyst bed, respectively. The term $h_f a_v(T_s - T_g)$ represents the heat transfer between the gas and solid phase, and the term $(1 - \varepsilon_b)\sum - \Delta H_{rxn,j}\eta_j R_j$ stands for the amount of heat released from, or added to, the surface due to the occurring reactions, where η_j is the so-called catalyst effectiveness factor for reaction j (see section SI.1 for more information). As written in the section Model Assumptions, we assume η_j is 1 in our model, but we keep this parameter in the above equation, so that this equation is also more generally valid, for other conditions.

In general, the temperature at the catalyst surface can be different from the bulk gas temperature. In the experiments to which our model is applied, the SEM micrographs before and after plasma showed no difference, since the Pt catalyst was at a distance of 15 cm from the tail of the active plasma area. This was in good agreement with the minimal temperature increase (i.e., 1−2 °C) that was experimentally observed at the catalyst surface upon plasma ignition,[13] so the time dependency of the surface temperature $\left(\frac{\partial T_s}{\partial \tau}\right)$ can be neglected. Therefore, the gas−solid heat transfer rate can analytically be calculated from eq 4 as follows:

$$h_f a_v(T_s - T) = (1 - \varepsilon_b)\sum \Delta H_{rxn,j}\eta_j R_j \tag{5}$$

(Ergun Equation for the Pressure Drop Across the Catalyst Bed (Equation 6). Modeling of gas flow through porous media is quite complex, but it can sometimes be considerably simplified if the porosity does not vary a lot and a uniform flow distribution within the bed can be assumed. In general, this is the case in fixed bed reactors, which are made up of roughly uniform particles in terms of both shape and size.

Gas flow through fixed beds can be modeled by analogy with flow in pipes when the bed porosity is uniform. There is however a pressure drop through a fixed bed, due to frictional losses and inertia, characterized by a linear and quadratic dependence on the flow velocity, respectively. Adding these two contributions to the gas flow equation results in the well-known Ergun equation for calculation of the pressure drop across a catalyst bed, which can be written in its dimensionless form as[27]

$$f_p = \frac{150}{Gr_p} + 1.75 \tag{6}$$

Here f_p and Gr_p are the fixed bed friction factor and modified Reynolds number, respectively, and they are defined as

$$f_p = \frac{\Delta p}{L}\frac{D_p}{\rho u_s^2}\left(\frac{\varepsilon^3}{1 - \varepsilon}\right) \tag{7}$$

$$Gr_p = \frac{\rho u_s D_p}{(1 - \varepsilon)\mu} \tag{8}$$

where Δp is the pressure drop (Pa) across the catalyst bed, L is the length of the catalyst bed (m), D_p is the equivalent spherical diameter of the packing (m), ρ is the density of the gas mixture (kg m^{-3}), μ is the dynamic viscosity of the gas mixture (kg (m s)$^{-1}$), u_s is the gas superficial velocity (m s^{-1}), and ε is the void fraction (porosity) of the catalyst bed.

Model Parameters. There are many physical properties used in our model, like mass transfer coefficient, heat transfer coefficient, axial dispersion coefficient, and effective thermal conductivity. Normally their values are unknown or sometimes very difficult to measure experimentally. Therefore, we use empirical correlations to determine these properties. According to the literature, those empirical correlations have already been successful in modeling of fixed bed reactors. The mass transfer coefficient is not used in our model, as the term accounting for mass transfer between gas and solid phase can be replaced by the adsorption rates calculated from the surface kinetics model (cf., explanations for eq 1 above). Similarly, the heat transfer coefficient is not used in our model, as it can be determined analytically (cf., explanation for eq 4 and 5 above). However, for systems with less information on the kinetics or with no control on the catalyst bed temperature, the calculation of these properties is crucial. Therefore, the conventional correlations that are normally used in modeling of fixed bed catalytic reactors for all the physical properties used in our model are presented in Supporting Information (section SI.1). Additionally, an overview of the other parameters used in the model is presented in Table 1.

As mentioned before, our modeling approach is developed for modeling of the catalytic bed of a two-stage plasma-catalytic reactor, where a reactive flow, generated from a remote plasma, is exposed to a catalytic bed. However, this approach can also be adapted to a single-stage plasma-catalytic reactor, where the plasma is in direct contact with the catalytic bed. In such a case, a more detailed plasma kinetics model should be considered for the gas phase, in which the presence of several different species like ions, electrons, and electronic and vibrationally excited species are considered. Of course, such a detailed plasma kinetics model will result in significant expansion of the mass transfer equations governing the plasma-catalytic system. In a single-stage plasma-catalytic system, a higher population of electronic and vibrationally excited species may enhance the dissociative adsorption reaction rates. Additionally, adsorption of other reactive species at the catalytic surface may occur, and therefore, their influence on improving or limiting the process toward the desired product should be carefully investigated. Furthermore, the effect of the presence of numerous species in the gas phase on the axial dispersion coefficient as well as on the physical and thermodynamic properties of the gas phase should also be considered. Moreover, the effect of plasma on the catalysts also needs to be investigated to make sure that the catalyst remains active. Finally, the electrical power, supplied to the gas phase to form a plasma, is an additional source of creating temperature gradients inside the system, and therefore, its effect should also be considered in the energy balance equations. All these effects

Table 1. Other Parameters Used in the Model, As Well As the References Where Their Values Are Taken From

parameter	name	value	unit	ref
P	pressure	0.005	bar	13
T_g	gas temperature	873	K	13
S	number of active sites	2.3×10^{-7}	mol	13
N_A	Avogadro's number	6.02×10^{23}	mol^{-1}	
R	gas universal constant	8.31	$J\ (K\ mol)^{-1}$	
M_{air}	molecular weight of air	28.97	$g\ mol^{-1}$	
Q_{in}	inlet gas volumetric flow rate	1.67×10^{-6}	$m^3\ s^{-1}$	13
$Q = Q_{in}\dfrac{T_g}{T°}\dfrac{P°}{P}$	actual gas volumetric flow rate	0.001	$m^3\ s^{-1}$	
V_p	total volume of catalyst particles	6.9×10^{-9}	m^3	13
d_{bed}	catalyst bed diameter	2.5×10^{-2}	m	13
$A_{bed} = \pi\dfrac{d_{bed}^2}{4}$	catalyst bed cross section area	4.91×10^{-4}	m^2	
$L = \dfrac{V_b}{A_{bed}}$	catalyst bed characteristic length	1.41×10^{-5}	m	
λ_s	solid thermal conductivity	2.5	$W\ (m\ K)^{-1}$	28
d_r	reactor diameter	3.4×10^{-2}	m	13
$A_r = \pi\dfrac{d_r^2}{4}$	reactor cross section area	9.08×10^{-4}	m^2	
$u_s = Q/A_r$	superficial gas velocity	1.11	$m\ s^{-1}$	
$V_t = A_{r}L$	total volume of catalyst bed	1.28×10^{-8}	m^3	
$t_{res} = \dfrac{V_t}{Q}$	residence time	1.27×10^{-5}	s	
ε_b	catalyst bed porosity	0.46	–	
d_{pore}	catalyst pores average diameter	10.4×10^{-9}	m	29
$\tau_{catalyst}$	catalyst tortuosity (see section SI.1)	1.57	–	
C_T	number of sites per unit area of the catalyst	1.46×10^{19}	m^{-2}	13
$a_v = \dfrac{1}{C_T V_p}$	external surface area per unit volume of the catalyst	9.87×10^{-12}	$m^2\ m^{-3}$	
C_{pg}	gas phase heat capacity	1.01×10^3	$J\ (kg\ K)^{-1}$	

are however outside the scope of this work, and will be considered in a follow-up study.

Initial and Boundary Conditions. The boundary conditions for this system of equations are as follows:

At the reactor inlet (inlet of the catalyst bed, $\zeta = 0$):

$$C_i = C_i^{after\ plasma},\ \frac{\partial C_{i,s}}{\partial \zeta} = 0,\ T = T_g,\ T_s = T_{bed},\ P = P_0 \tag{9}$$

At the catalyst bed outlet ($\zeta = 1$):

$$\frac{\partial C_i}{\partial \zeta} = \frac{\partial C_{i,s}}{\partial \zeta} = 0,\ \frac{\partial T_s}{\partial \zeta} = \frac{\partial T}{\partial \zeta} = 0 \tag{10}$$

The initial conditions are defined as

$$\left(C_{i,0} = C_i^{after\ plasma},\ C_{i,s,0} = 0,\ T_0 = T_g,\ T_{s,0} = T_{bed}\right) \tag{11}$$

Reaction Kinetics. We only consider the most important reactions for NO production, describing N_2, O_2, N, O, and NO. In order to account for the simultaneous effects of plasma and catalyst on the system behavior, the plasma-catalytic N_2 oxidation kinetics model proposed by Ma et al. is also used in the present study.[13] As the catalytic N_2 oxidation is the reverse of the more widely studied catalytic NO decomposition reaction, a surface kinetics model relevant to NO decomposition on Pt is used to describe the catalytic reactions (Table 2).

Table 2. Surface Reactions Included in the Model, along with Their Reaction Parameters[30][a]

reaction no.	reaction on Pt (211) surface	ΔH (eV)	E_a (eV)
R_1	$N_2 + 2^* \rightleftarrows 2N^*$	1.35	2.55
R_2	$O_2 + 2^* \rightleftarrows 2O^*$	−2.09	0.17
R_3	$N +^* \rightleftarrows N^*$	−4.26	0.00
R_4	$O +^* \rightleftarrows O^*$	−3.66	0.00
R_5	$N^* + O^* \rightleftarrows NO^* +^*$	−0.61	1.39
R_6	$NO^* \rightleftarrows NO +^*$	1.89	1.89

[a]Note that * stands for an empty surface site. ΔH: Reaction enthalpy, E_a: Activation energy.

The activation energy for dissociation of N_2 and O_2 in the gas phase is quite high (i.e., 9.74 and 5.12 eV, respectively), so dissociation in the gas phase is unlikely to occur at the conditions under study. Therefore, the dissociation reactions of N_2 and O_2 were excluded from the reactions describing the gas phase reaction kinetics. Additionally, due to the very low concentration of N and O radicals in the gas phase and the zero activation energy for their adsorption on the catalyst surface (cf., Table 2), we assume that they will immediately adsorb on the surface upon their entrance to the catalyst bed, and thus their recombination back to N_2 and O_2 in the gas phase can be neglected in the catalytic stage of the reactor under study. Therefore, in the gas phase, we only consider the so-called Zeldovich mechanism to occur, which describes the noncatalytic N_2 oxidation (Table 3). To add the effect of vibrationally excited N_2 and O_2 molecules, formed in the plasma, on the proposed reaction kinetics, the normalized density of each vibrationally excited state is determined considering a Treanor vibrational distribution function.[3,31] We assume that N_2 and O_2 have the same vibrational temperature. Ma et al. estimated vibrational temperatures to be 10000 K in the plasma, based on ref 32, and they selected $T_v = 6000$ K as a representative vibrational temperature after the temperature drop expected during the flow of the postplasma gas flow to the catalyst bed.[13] Therefore, we also use $T_v = 6000$ K in our model. Details on the calculation of the plasma-catalytic reaction rate coefficients are presented in Supporting Information (section SI.2) following the methods described by Mehta et al.[33]

Note that NO_2 formation can also be one of the possible pathways in this system. However, in the present work we do not consider (catalytic) NO_2 formation since to our knowledge the kinetic parameters (i.e., reaction barriers and enthalpies on Pt) needed for our model were not available in the literature. Additionally, no experimental measurements of NO_2 were reported by Ma et al.,[13] which is used to benchmark our model.

Table 3. Gas-Phase Reactions Included in the Model, along with Their Reaction Parameters[34a]

reaction no.	reaction	A (cm³ s⁻¹)	E_a (eV)	ΔH (eV)	ΔS (meV K⁻¹)
R_7	$N_2 + O \rightleftarrows NO + N$	3.0×10^{-10}	3.31	3.26	0.123
R_8	$O_2 + N \rightleftarrows NO + O$	$3.2 \times 10^{-12}\left(\dfrac{T}{300}\right)$	0.27	−1.38	0.139

[a]These two reactions form the so-called Zeldovich mechanism of NO formation.[35] A: Pre-exponential factor. E_a: Activation energy. ΔH: Reaction enthalpy. ΔS: Reaction entropy.
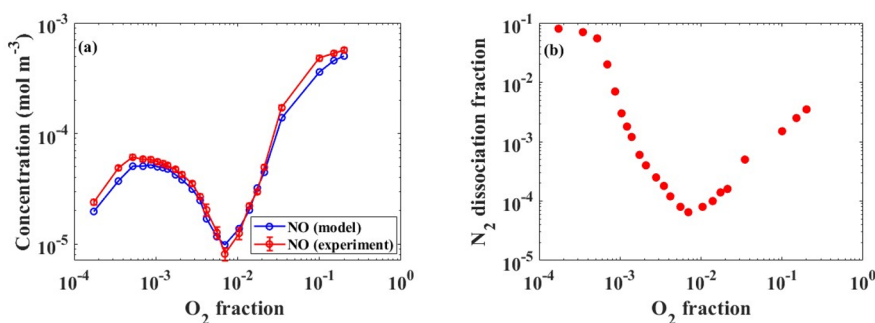
Figure 3. (a) Comparison of experimental and calculated NO concentration at the reactor outlet, as a function of O_2 fraction in the feed gas. In (b) the assumed N_2 dissociation fraction is plotted as a function of O_2 fraction in the feed gas, for which our model can reproduce the experimental trends of NO concentration as illustrated in (a). Such a nonmonotonic variation in N_2 dissociation fraction as a function of O_2 fraction is indeed also described in the literature (see text), indicating that our model can reproduce the experimental NO concentration within a realistic input parameter space.

Typical Calculation Results. The model calculates the concentrations of the various species in the model (both in the gas phase and at the catalyst surface) and the reaction rates of all reactions listed in Tables 2 and 3, both as a function of time and position across the catalyst bed, for a wide range of conditions. This allows us to determine the underlying mechanisms. Of special interest is the NO concentration at the reactor outlet, as this is the final product, which we try to optimize.

Finally, based on the total power introduced in the system, and the total NO concentration at the reactor outlet, we can in principle also calculate the energy cost of NO formation as

$$EC = \frac{P_{total}}{C_{NO} \times Q} \times 10^{-6} \tag{12}$$

where EC is the energy cost of NO formation (MJ mol⁻¹), P_{total} is the total power (W), C_{NO} is the NO concentration (mol m⁻³) at the reactor outlet, Q is the gas volumetric flow rate (m³ s⁻¹), and 10^{-6} is the conversion factor from J to MJ.

Note, however, that we cannot calculate the absolute value of the energy cost, as we do not know the exact power going into the system. Indeed, it consists of the power of the power supply, heating mantle of the catalyst bed, and vacuum pump, and the values of the latter two were not reported in the study of Ma et al.[13] Therefore, we will plot the energy cost in arbitrary numbers, so that we can study the relative trends of the energy efficiency of the system for various conditions, and because the total power going into the system will be (more or less) constant for all conditions, keeping in mind that the power of the power supply is constant, as well as the temperature of the catalyst bed and the pressure (i.e., flow rate of the vacuum pump).

■ RESULTS AND DISCUSSION

Effect of Postplasma Species Fluxes Entering the Catalyst Bed. To evaluate the NO production sensitivity to

the postplasma fluxes of species entering the catalytic stage, we solved our model for a wide range of postplasma concentrations of the species involved in the NO production process. It allows us to estimate for which conditions our model can reproduce the experimental NO concentrations, reported by Ma et al.[13] In addition, this parameter study gives us insights in how the reaction performance in the catalyst bed is affected by the postplasma composition.

We used the partial differential equation (PDE) solvers in MATLAB & Simulink 2022 for solving eqs 1−4. Note that using the dimensionless form of eqs 1−4, although it has no influence on the quantitative results of our model, helps a lot in better defining the governing equations for MATLAB & Simulink PDE solvers. Therefore, the procedure for deriving these dimensionless equations is discussed in section SI.3. In our model, linear and nonlinear PDEs, algebraic equations, as well as initial and boundary conditions are involved. We first checked the sensitivity of the model for discretization, ranging from 10 to 1000 intervals, and the model results were found independent of discretization for discretization intervals above 100. Hence, the catalyst bed of the experimental reactor was axially discretized by 100 uniform intervals, and the output results are reported after 1260 s (or 21 min), when steady state was definitely reached.

According to the literature, at similar plasma conditions to the reactor under study, when $\log_{10} x_{O_2}$ varies from −4 to −1 (i.e., the O_2 fraction in the feed gas varies from 10^{-4} to 10^{-1}), the $\log_{10}\frac{P_N}{2P_{N_2}}$ (i.e., the logarithm of the N_2 dissociation fraction) can vary nonmonotonically or decrease monotonically, in a range from −4 to −2.5.[13,36−38] We solved our model for a wide range of N_2 dissociation fractions between 10^{-5} and 10^{-1} to completely cover the reported range in the literature at different O_2 fractions in the feed gas corresponding to the experiments of Ma et al.[13] Knowing the postplasma concentration of NO as a function of O_2 fraction in the feed
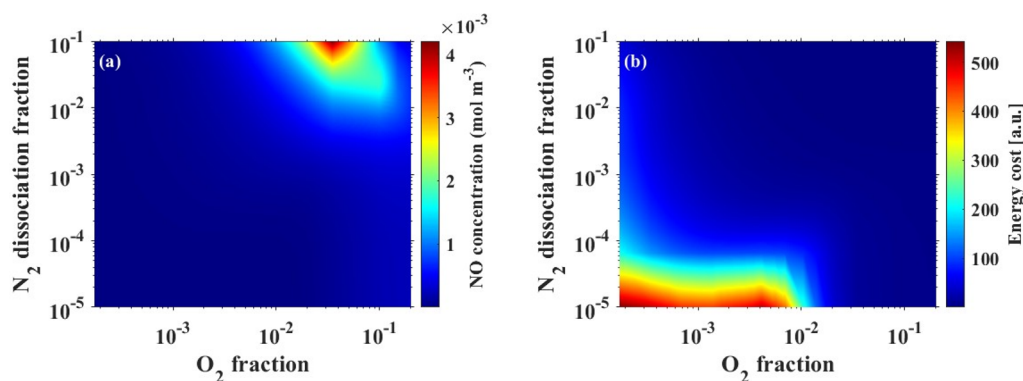
Figure 4. Effect of N_2 dissociation fraction and O_2 fraction in the feed gas, on the NO concentration (a), and its corresponding energy cost of formation (b) calculated by the model.

gas, as reported by Ma et al.,[13] and assuming that the O_2 dissociation fraction in the plasma is normally 1 order of magnitude greater than for N_2,[32,39−42] the postplasma concentration of each species can be calculated as a function of N_2 dissociation fraction, at different O_2 fractions in the feed gas, as described in SI.4. Note that the results presented below are strongly influenced by the assumption of a constant ratio between O_2 and N_2 dissociation fraction. Of course, this factor 10 is just an approximation, based on the literature, and we do not know the exact value. Therefore, we keep this parameter constant in our calculations.

Figure 3a illustrates the experimental and calculated NO concentration at the reactor outlet, as a function of O_2 fraction in the feed gas. According to the experiments reported by Ma et al.,[13] for an O_2 fraction below 0.001, increasing the O_2 fraction in the feed gas results in a slight increase in the NO concentration until it reaches a maximum at an O_2 fraction around 0.001 (see Figure 3a). By further increasing the O_2 fraction in the range from 0.001 to 0.01, the NO concentration starts to drop until it reaches a minimum at an O_2 fraction of about 0.01. Finally, when the O_2 fraction rises to 0.2, the NO concentration also rises drastically. Capturing these trends by our model requires a precise measurement of all different species concentrations in the postplasma gas flow that enters the catalyst bed, as these values are used as the initial conditions of our model. However, these data were not available for our case study. Hence, for a certain O_2 fraction in the feed gas (which automatically determines the N_2 fraction), we had to assume a certain N_2 dissociation fraction (which determines the O_2 dissociation fraction, as explained above). Together, they determine the N_2, O_2, N, and O concentrations (or fluxes) in the postplasma mixture (cf., section SI.4). When assuming an N_2 dissociation fraction profile as a function of O_2 fraction in the feed gas as illustrated in Figure 3b, which qualitatively captures the behavior described in literature (see above), our model can reproduce with reasonable accuracy the observed experimental trend for the measured NO concentrations at the reactor outlet as a function of O_2 fraction (see Figure 3a).

To further investigate how the postplasma gas composition affects the reaction performance in the catalyst bed, we plot in Figure 4 the NO concentration (a) and its corresponding energy cost of formation (b) calculated by our model at different N_2 dissociation fractions, as a function of O_2 fraction in the feed gas. Note that the energy cost is plotted in arbitrary

numbers, as explained above, so we can also compare the relative trends for various conditions.

As observed in Figure 4a, the NO production is not really sensitive to the N_2 dissociation fraction at low O_2 fractions in the feed gas (i.e., x_{O_2} < 1%). The reason is that the number of O radicals in the gas flow entering the catalyst bed, and subsequently their concentration at the catalyst surface, is so low that not much NO can be produced through the catalytic process. However, at higher O_2 fractions in the feed gas (i.e., x_{O_2} > 1%).), high N_2 dissociation fractions yield a high NO concentration at the reactor outlet, as observed in Figure 4a. On the other hand, the NO concentration is still low at a low N_2 dissociation fraction. Indeed, at these higher O_2 fractions, the concentration of O_2 and O radicals in the postplasma gas flow is higher, and therefore more O radicals can be adsorbed on the catalyst surface, which can then react with the surface-adsorbed N radicals to form NO through the associative recombination reaction (R_5). However, even when enough surface-adsorbed O radicals exist at the catalyst surface, only a low amount of NO can be produced at low N_2 dissociation fractions, due to the low concentration of N radicals in the gas phase and subsequently, at the catalyst surface. This explains why the NO production at the catalytic stage is very sensitive to the N_2 dissociation fraction. As a result, the energy cost of NO production is higher at lower N_2 dissociation fractions; Figure 4b, while upon increasing the N_2 dissociation fraction, the energy cost of NO production decreases for N_2 dissociation fractions close to 0.1, at an O_2 fraction of 20% in the feed gas (Figure 4b).

In summary, a high N_2 dissociation fraction (and thus also a high O_2 dissociation fraction, as they are connected: the latter is typically 1 order of magnitude higher), in combination with a relative high O_2 fraction (∼20%) in the feed gas, yields a high NO concentration at the reactor outlet and a lower energy cost of formation (while the opposite conditions give rise to a low NO concentration and high energy cost). This is logical, because these conditions produce more O and N radicals, which are the main drivers of NO production at the catalyst surface. Indeed, we performed a detailed reaction analysis to determine the dominant mechanisms toward NO production, and the results are presented in the Supporting Information (sections SI.5 to SI.9).

We also varied the postplasma concentration of NO in a range from 0 to 6.8×10^{-4} mol m^{-3} (i.e., 10000 ppm) to investigate the effect of NO concentration entering the catalyst bed on the NO concentration at the reactor outlet (Figure 5).
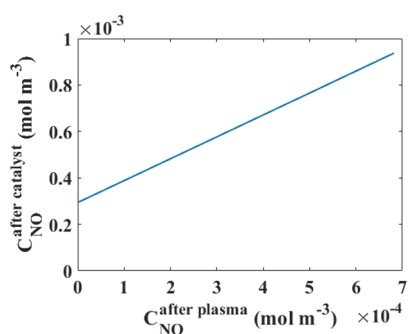
Figure 5. Effect of NO concentration entering the catalyst bed on the NO concentration at the reactor outlet (T_g = 873 K, x_{O_2} = 20%, P_{plasma} = 80 W, T_v = 6000 K, P = 5 mbar, N_2 dissociation fraction = 3.5 × 10^{-3}).

This study was performed for an N_2:O_2 mixture of 80:20 at an N_2 dissociation fraction of 3.5 × 10^{-3}, for which our model can reproduce the experimental NO concentration at the reactor outlet. An O_2 fraction of 20% was chosen, as the catalytic effect is still pronounced enough at this condition (comparing 2.2 × 10^{-4} mol m^{-3} (3200 ppm) and 5.7 × 10^{-4} mol m^{-3} (8250 ppm) for plasma only and plasma-catalytic processes in the experiments of Ma et al.,[22] respectively). Additionally, this feed gas mixture mimics dry air composition, and is therefore of special interest for industrial purposes. As illustrated in Figure 5, even without NO present in the postplasma gas, about 3 × 10^{-4} mol m^{-3} of NO is produced at the catalyst bed, due to reactions of N, O, N_2 and O_2 at the catalyst surface. Furthermore, a linear dependence is observed for the NO concentration at the reactor outlet as a function of postplasma concentration of NO. Hence, the total NO concentration at the reactor outlet is the sum of the NO formed in the plasma and a constant amount of 3 × 10^{-4} mol m^{-3} formed at the catalyst bed.

Effect of Back-Mixing Degree. Increasing the desired product yield (NO in our case) is always the main purpose in design and optimization of any reactor. Figure 6 shows how the NO concentration at the reactor outlet and its energy cost of formation vary with the degree of back-mixing inside the reactor. To this end we solved the model for different Pe numbers (i.e., different axial dispersion coefficients) ranging from 10^{-3} (corresponding to D_z = 1.6 × 10^{-2} m^2 s^{-1}, close to CSTR) to 550 (corresponding to D_z = 2.8 × 10^{-8} m^2 s^{-1} close to PFR). Note that for other calculations, the value of the Pe number is calculated based on the operating conditions of the

experiment, and was found to be equal to 502, indicating that our system can be described as a PFR, with negligible back-mixing. That also explains why in Figure 5, the plasma-produced NO is additive to the NO produced in the catalytic bed, and no NO from the plasma phase is lost by reactions in the catalytic bed.

As illustrated in Figure 6, less back-mixing (i.e., high Pe, close to PFR) yields a rise in the NO production (Figure 6a) and a drop in its energy cost of formation (Figure 6b). We observe an S shape pattern with increasing Pe number from CSTR to PFR conditions (Figure 6a). The reason is that at lower back-mixing degrees the catalytically produced NO has less tendency to intermix with unreacted species, and therefore, its loss due to axial dispersion decreases. This clearly confirms the adverse effect of back-mixing on the NO concentration at the reactor outlet. Hence, to reduce this adverse effect, the reactor and the catalyst bed size and configuration should be optimized to minimize the degree of back-mixing (i.e., flow pattern as close as possible to a PFR).

Effect of the Catalyst Bed Characteristic Length. We varied the total volume of catalyst particles from 6.9 × 10^{-9} m^3 (i.e., total volume of catalyst in the experimental setup) to 10^{-3} m^3. As the diameter of the catalyst bed is considered to be constant, this results in an increase in the characteristic length of the catalyst bed from 14 μm to 2 m. It should be noted that a characteristic length of 2 m is not realistic in practice, but we performed the simulations in this wide range to show trends. The contact time of the gas with the catalyst (see SI.10: Figure S7a) rises from 10^{-5} s (for the smallest catalyst volume of 6.9 × 10^{-9} m^3, corresponding to the experiments, i.e., characteristic length of 14 μm) to 1.8 s (for the largest catalyst volume investigated of 10^{-3} m^3, corresponding to a characteristic length of 2 m). Normally, increasing the contact time of the gas with the catalyst should result in a higher NO concentration. However, as illustrated in Figure 7a, increasing the characteristic length (i.e., a longer contact time of the gas with the catalyst) results in a lower NO concentration until a minimum is reached at around 1 mm. This is because the increase in characteristic length of the catalyst bed promotes the adsorption of NO and its subsequent dissociation into N and O radicals on the surface (i.e., the net rates of associative recombination (R_5) and NO desorption (R_6) on and from the surface, respectively, dramatically drop, Figure S7b). Therefore, at this range when the characteristic length increases from 14 μm to around 1 mm, the NO production rate at the reactor outlet (expressed in mol m^{-3} s^{-1}) sharply decreases from values around 17 to 0.02 mol m^{-3} s^{-1} (Figure 7b). As a result,
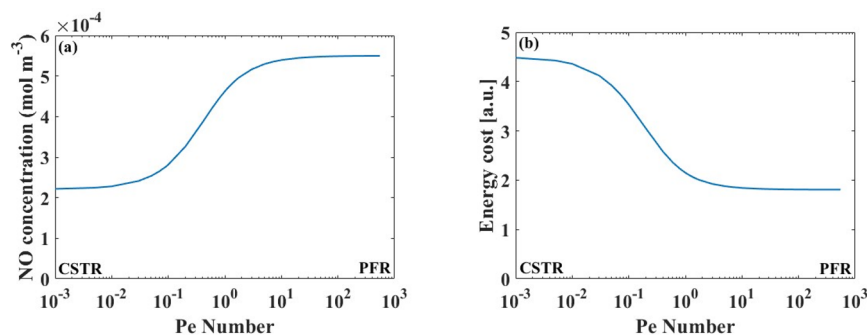

Figure 6. Effect of Pe number on the outlet concentration of NO (a), and its energy cost of formation (b) (T_g = 873 K, x_{O_2} = 20%, T_v = 6000 K, P = 5 mbar, N_2 dissociation fraction = 3.5 × 10^{-3}).
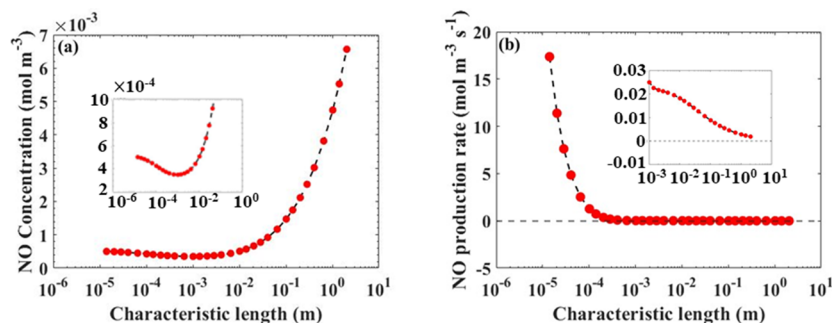
Figure 7. Effect of the catalyst bed characteristic length on the NO concentration (a), and the net NO reaction rate (b), at T_g = 873 K, x_{O_2} = 20%, T_v = 6000 K, P = 5 mbar, N_2 dissociation fraction = 3.5×10^{-3}. The insets in (a) and (b) are zoom-in plots of NO concentration and production rate as a function of characteristic length, respectively, in the ranges where their trends, as a function of characteristic length, are not clearly visible.
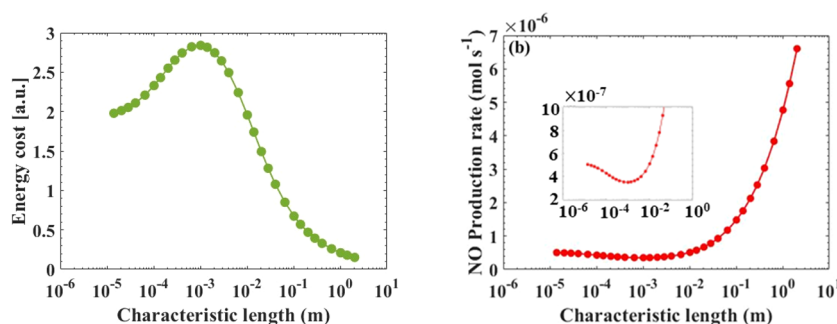

Figure 8. Effect of the catalyst bed characteristic length on the energy cost of NO formation (a), and the NO production rate (b), at T_g = 873 K, x_{O_2} = 20%, T_v = 6000 K, P = 5 mbar, N_2 dissociation fraction = 3.5×10^{-3}. The inset in (b) is the zoom-in plot of NO production rate as a function of characteristic length in a range where its trend, as a function of characteristic length, is not clearly visible.

a longer contact time (Figure S7a) is not enough to compensate for the effect of the sharp drop in NO production rate, and to help the process toward more production of NO. Therefore, less NO is produced and its concentration, at the outlet of the reactor, is lower at longer characteristic lengths (Figure 7a). By further increasing the characteristic length of the catalyst bed to values above 1 mm, the NO production rate continues to drop, but this drop is significantly less steep than for shorter characteristic lengths. Simultaneously, the contact time continues to rise with increasing characteristic length (Figure S7a). At these long characteristic lengths (longer than 1 mm), the improvements in contact time of the gas with the catalyst are significant enough to promote the process toward more NO production. In other words, although the NO is produced at lower rates, for longer characteristic lengths the contact time of the gas with the catalyst is long enough to enhance the NO concentration at the reactor outlet (Figure 7a).

The effect of the catalyst bed characteristic length on the energy cost of NO formation and on the NO production rate (in mol s^{-1}) is illustrated in Figure 8, panel a and b, respectively. Increasing the catalyst bed characteristic length has no effect on the gas volumetric flow rate. Therefore, the NO concentration is the only variable that determines the NO production rate (the product of NO concentration and the gas volumetric flow rate, i.e., denominator of eq 12), and thus it follows exactly the same trend as the NO concentration (Figure 8b). Similar to the NO concentration, the NO production rate decreases with increasing characteristic length until it reaches a minimum at around 1 mm (Figure 8b). As a result, the energy cost of NO formation increases upon

increasing characteristic length of the catalyst bed from 14 μm (corresponding to the experimental conditions) 1 mm (Figure 8a). After this minimum in production rate (or maximum in energy cost), further increasing the characteristic length results in a higher NO concentration, and hence, the NO production rate also increases. As a result, the energy cost of NO formation decreases toward a characteristic length of 2 m (i.e., around 92% improvement).

Such an improvement in energy cost of NO formation might lead to the conclusion that longer catalyst beds significantly improve the process performance. However, such long characteristic lengths (2 m, using 10^{-3} m^3 of the porous Pt catalyst) are not feasible due to the limitations in configuration of the reactor under study and laboratory conditions. This can explain the reasoning behind selection of 14 μm as the characteristic length of the catalyst bed in the experiments, in addition to the fact that it also requires only a limited amount of catalyst. Nevertheless, these results illustrate that our 1D heterogeneous catalysis model allows to investigate the optimum length of the catalyst bed, which is not possible by a CSTR model.

Effect of Catalyst Bed Porosity. In the reactor configuration under study, the catalyst bed porosity can easily be adjusted by varying the diameter of the catalyst bed (i.e., the diameter of the YSZ support), which can affect the performance. In our model, we varied the catalyst bed porosity from 0.06 (corresponding to a catalyst bed diameter of 33 mm) to 0.99 (corresponding to a catalyst bed diameter of 3 mm). The experiments were performed with a porosity of 0.46, cf. Table 1. Note that by increasing the catalyst bed diameter from 3 to 33 mm, the characteristic length of the catalyst bed
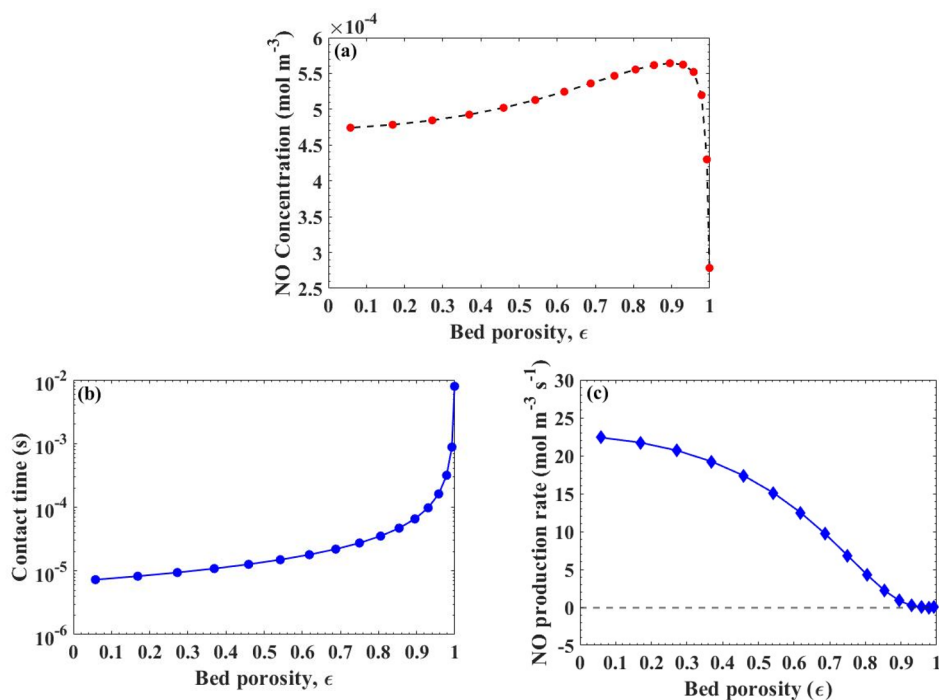
Figure 9. Effect of the catalyst bed porosity on the NO concentration (a), the contact time between gas and catalyst (b), and net NO production rate (c), at T_g = 873 K, x_{O_2} = 20%, T_g = 6000 K, P = 5 mbar, N_2 dissociation fraction = 3.5×10^{-3}.
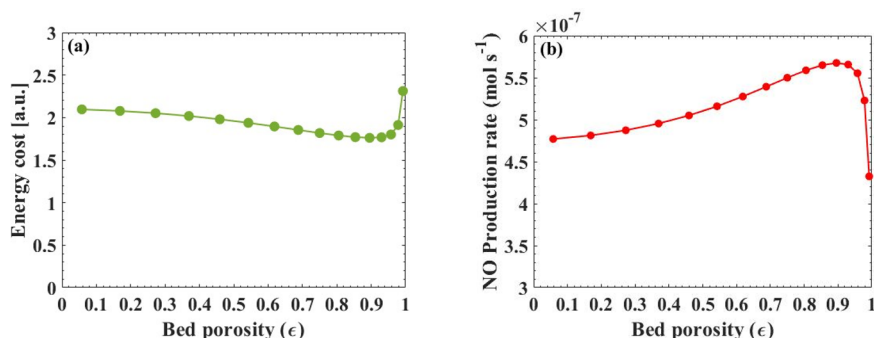

Figure 10. Effect of catalyst bed porosity on the energy cost of NO formation (a), and the NO production rate (b), at T_g = 873 K, x_{O_2} = 20%, T_v = 6000 K, P = 5 mbar, N_2 dissociation fraction = 3.5×10^{-3}.

decreases from 1 mm to 8.1 μm. The effect of catalyst bed diameter on the characteristic length and on the porosity of the catalyst bed is explained in the Supporting Information, section SI.11.

Figure 9a shows the effect of the bed porosity on the NO concentration at the outlet of the catalyst bed at steady state. A higher bed porosity means that there is more free volume in the catalyst bed for the gas to pass through. Also, the higher the porosity, the longer the characteristic length of the catalyst bed. Therefore, more volume of the gas passes through a longer catalyst bed, which significantly improves the contact time of the gas with the catalyst particles inside the bed (Figure 9b). On the other hand, as the porosity increases (i.e., at longer catalyst bed characteristic lengths), the NO production rate decreases (Figure 9c) due to more NO adsorption and subsequent dissociation on the catalyst surface (cf., the results presented for the effect of catalyst bed characteristic length). It is clear from Figure 9a that a higher bed porosity results in a higher NO concentration at the outlet of the catalyst bed, until it reaches its maximum at porosity values around 0.9. The

reason is that, although at higher porosity values the NO reaction rate decreases a lot (Figure 9c), the higher contact time between gas and catalyst compensates for this drop in NO production rate. Therefore, the overall produced NO at steady state increases with increasing catalyst bed porosity. However, further increasing the bed porosity to values close to 1 means there is almost no catalyst inside the bed anymore (i.e., the effect of surface reactions become negligible), and as a result, the NO concentration at the outlet significantly drops.

To further investigate the effect of the catalyst bed porosity on the performance of the system, we plot in Figure 10a the energy cost of NO formation as a function of bed porosity. Increasing the catalyst bed porosity has no effect on the gas volumetric flow rate. Therefore, similar to the case of varying the catalyst bed characteristic length, the steady state NO concentration at the reactor outlet is the only parameter that controls the NO production rate in mol s^{-1} (i.e., product of the NO concentration and the gas volumetric flow rate), and subsequently, the energy cost of NO formation. As the porosity of the bed increases, the steady state NO concentration at the

reactor outlet increases until it reaches its maximum at porosity values around 0.9 (Figure 9a). As a result, the energy cost (Figure 10a) drops from $\varepsilon = 0.06$ (corresponding to $d_{bed} = 33$ mm) to $\varepsilon = 0.9$ (corresponding to $d_{bed} = 11$ mm). After this optimum porosity of 0.9, further increasing the catalyst bed porosity to values close to 1 leads to a significant drop in the NO concentration at the reactor outlet, and subsequently the NO production rate sharply drops (Figure 10b). Therefore, the energy cost of NO formation increases from $\varepsilon = 0.9$ to $\varepsilon = 0.99$.

According to our model predictions for the effect of catalyst bed porosity on the NO concentration and its energy cost of formation, further improvement in the performance may be possible by increasing the porosity of the catalyst bed from 0.46 (corresponding to the experiments) to 0.9. However, achieving such a high catalyst bed porosity might be difficult in practice. Note that increasing the porosity to these high values in our model was only possible because of the specific configuration of the catalyst bed in the reactor under study. In conventional (commercial) fixed bed reactors, where the catalyst bed is made of roughly uniform catalyst beads, the porosity range is typically quite narrow ($0.35 < \varepsilon < 0.55$).[43] Therefore, from a practical perspective, the selected porosity value in the experiments seemed to be among the best values possible in practice. Nevertheless, our calculations provide useful insights into the effect of this parameter, insofar that it can be tuned, and maybe our work can inspire experimental groups to design a catalytic bed with higher porosity.

CONCLUSIONS

Plasma-based NO production has recently gained increased interest as a potential sustainable alternative N_2 fixation process. Plasma catalysis can potentially enhance the performance by coupling a plasma with a (postplasma) catalytic surface. Mathematical modeling can play a key role in the optimization of the process, but modeling of plasma-catalytic N_2 fixation into NO is poorly studied.

In the present work, we developed a 1D heterogeneous catalysis model with axial dispersion (i.e., so-called axial dispersion model; ADM) for plasma-catalytic NO production in an ICP reactor. By considering the major transport phenomena in the catalytic bed (i.e., mass, energy and momentum transfer), the model allows one to gain valuable insight into the underlying mechanisms due to coupling of plasma and catalyst, and how to improve the performance. We studied the chemical reactions leading to the production of NO, and the resulting NO concentrations, both at the catalyst surface and in the gas phase, as a function of time and axial position in the reactor.

We investigated the effect of the postplasma composition (i.e., species concentrations/fluxes) on the NO concentration at the reactor outlet and its energy cost of formation. For this purpose, we varied (i) the N_2 dissociation fraction (which also determines the O_2 dissociation fraction, as the latter is typically an order of magnitude higher) and (ii) the O_2 fraction in the feed gas. Together, they determine the postplasma concentrations (or fluxes) of N, O, N_2 and O_2. In addition, we also studied the effect of varying the NO postplasma concentration on the NO concentration at the reactor outlet. In general, our model predicts that a higher N_2 dissociation fraction in the postplasma gas flow leads to a higher NO concentration at the reactor outlet. However, the NO production is not very sensitive to the N_2 dissociation fraction at O_2 fractions less

than 1% in the feed gas. A higher O_2 fraction in the feed gas and N_2 dissociation fraction in the postplasma gas flow result not only in a higher NO concentration, but also in a significant improvement in energy cost calculated by our model. Finally, a linear increase in the outlet concentration of NO was observed with a rise in the postplasma concentration of NO for a constant O_2 fraction in the feed gas, but also without NO in the postplasma mixture, a considerable amount of NO is formed at the catalyst bed, as the N and O radicals are the main drivers of catalytic NO production.

We also studied the effect of back-mixing on the NO production. Our model predicts that higher Pe numbers (i.e., flow patterns close to a PFR and therefore, lower back-mixing) lead to a higher concentration of NO at the reactor outlet and a drop in the process energy cost. Hence, for process improvement, it will be important to design a catalytic bed reactor resembling as much as possible a PFR.

Increasing the catalyst bed characteristic length in general leads to a high NO concentration and low energy cost, at least for very long characteristic lengths (around 2 m). Although a such value might be unrealistic and would require much more catalyst than the characteristic length used in the experiments, our simulations can provide information on the effect of this parameter on the system performance. Finally, increasing the catalyst bed porosity also results in a higher NO concentration and lower energy cost, until reaching a maximum at porosity values around 0.9. At still higher catalyst porosity, there would be almost no catalyst inside the bed, and therefore the effect of surface reactions would become negligible.

This kind of model has been used before in the field of thermal catalysis, and its robustness in simulation and optimization of various catalytic processes was already demonstrated.[21,22,44−46] However, in this paper, for the first time, we developed such a model for the simulation of a plasma-catalytic process for NO production. Our modeling approach can provide useful insights into the underlying mechanisms responsible for NO production, as a function of time and at different positions across the catalyst bed. Additionally, it can predict the effect of different operating parameters on the NO concentration at the reactor outlet and its energy cost of formation. Although these model predictions will need to be verified experimentally, and we do not claim the model predictions are quantitatively accurate, at least the results give insights into qualitative trends, when varying certain parameters.

Finally, this type of model is not only useful for explanation and improvement of the system under study, but also can be used for other plasma types coupled with a catalyst. Therefore, this modeling approach can open new windows of opportunity for the simulation, improvement, and optimization of plasma-catalytic processes operating in fixed bed reactors, not limited to N_2 fixation, but for various plasma-catalytic gas conversion processes.

ASSOCIATED CONTENT

Ⓢ Supporting Information

The Supporting Information is available free of charge at https://pubs.acs.org/doi/10.1021/acssuschemeng.2c05665.

> Technical details and empirical correlations for the calculation of physical properties in the model; calculation of adsorption, desorption, and surface reaction rate coefficients; dimensionless equations;

measured NO and calculated N_2, O_2, N, and O concentrations entering the catalyst bed; dominant mechanisms toward NO production; species concentration to explain the NO production mechanisms; temporal behavior of the net reaction rates at different positions across the catalyst bed; species formation and loss rates in the axial direction; heat transfer analysis; effect of catalyst bed characteristic length on the contact time of the gas with the catalyst, as well as surface and gas phase reactions; effect of catalyst bed diameter on the porosity and characteristic length of the catalyst bed (PDF)

■ AUTHOR INFORMATION

Corresponding Authors

Annemie Bogaerts − *Department of Chemistry, Research Group PLASMANT, University of Antwerp, BE-2610 Wilrijk-Antwerp, Belgium;* ⊙ orcid.org/0000-0001-9875-6460; Email: annemie.bogaerts@uantwerpen.be

Hamid Ahmadi Eshtehardi − *Department of Chemistry, Research Group PLASMANT, University of Antwerp, BE-2610 Wilrijk-Antwerp, Belgium; Research Group 4MAT, Université Liberé De Bruxelles, 1050 Brussels, Belgium;* ⊙ orcid.org/0000-0002-2985-0872; Email: Hamid.AhmadiEshtehardi@uantwerpen.be

Authors

Kevin Van 't Veer − *Department of Chemistry, Research Group PLASMANT, University of Antwerp, BE-2610 Wilrijk-Antwerp, Belgium; Chemistry of Surfaces, Interfaces and Nanomaterials (ChemSIN), Faculty of Science, Université Libre De Bruxelles, 1050 Brussels, Belgium;* ⊙ orcid.org/0000-0003-2540-467X

Marie-Paule Delplancke − *Research Group 4MAT, Université Liberé De Bruxelles, 1050 Brussels, Belgium*

Francois Reniers − *Chemistry of Surfaces, Interfaces and Nanomaterials (ChemSIN), Faculty of Science, Université Libre De Bruxelles, 1050 Brussels, Belgium*

Complete contact information is available at:
https://pubs.acs.org/10.1021/acssuschemeng.2c05665

Notes

The authors declare no competing financial interest.

■ NOMENCLATURE

a_v	External surface area per unit volume of the catalyst (m^2 m^{-3})
A_{bed}	Cross section surface area of the catalyst bed (m^2)
A_r	Reactor cross section surface area (m^2)
C_i	Concentration of species i in the gas phase (mol m^{-3})
$C_{i,s}$	Concentration of species i in the solid phase (mol m^{-3})
C_{pg}	Heat capacity of the gas phase (Jkg^{-1} K^{-1})
$C_{p,bed}$	Heat capacity of the catalyst bed (Jkg^{-1} K^{-1})
C_T	Number of sites per unit volume of the catalyst
D_z	Axial dispersion coefficient (m^2 s^{-1})
D_p	Equivalent spherical diameter of the packing (m)
D_m	Average molecular diffusivity (m^2 s^{-1})
D_i	Effective diffusion coefficient (m^2 s^{-1})
D_{Amix}	Molecular diffusion coefficient of species A in the gas mixture (m^2 s^{-1})
D_{AB}	Binary molecular diffusion coefficient (m^2 s^{-1})
D_{Kn}	Knudsen diffusion coefficient (m^2 s^{-1})
d_{pore}	Diameter of catalyst pores (m)
d_p	Diameter of catalyst particles (m)
d_{bed}	Diameter of the catalyst bed (m)
d_r	Reactor diameter (m)
E_a	Activation energy (eV)
f_p	Fixed bed friction factor
G_{rp}	Modified Reynolds number of the fixed bed
G_s	Mass velocity of the gas phase (kg m^{-2} s^{-1})
h_f	Heat transfer coefficient (Wm^{-2} K^{-1})
$j_{D,i}$	Chilton-Colburn factor for mass transfer
j_H	Chilton-Colburn factor for heat transfer
$k_{g,i}$	Gas-to-solid mass transfer coefficient (m^{-3} m^{-2} s^{-1})
L	Length of the catalyst bed (m)
M	Molecular weight (g mol^{-1})
Nu	Nusselt number
Pr	Prandtl number
P	Pressure (Pa)
$P°$	Standard pressure
Q_{in}	Inlet gas volumetric flow rate (m^3 s^{-1})
Q	Actual gas volumetric flow rate (m^3 s^{-1})
r_i^{gas}	Rate of formation or destruction of species i in the gas phase (mol m^{-3} s^{-1})
r_i^s	Rate of formation or destruction of species i in the solid phase (mol m^{-3} s^{-1})
R_j	Rate of reaction of species i (mol m^{-3} s^{-1})
R	Gas universal constant (Pa m^3 mol^{-1} K^{-1})
Re	Reynolds number
S	Number of active sites on the catalyst surface (mol)
Sh	Sherwood number
Sc	Schmidt number
t	Time (s)
t_{res}	Residence time (s)
T_s	Surface temperature of the catalyst (K)
$T°$	Standard temperature
T_g	Gas temperature (K)
T_v	Vibrational temperature (K)
u_s	Gas superficial velocity (m s^{-1})
V_p	Total volume of the catalyst particles (m^3)
V_t	Total volume of the catalyst bed (m^3)
x_i	Mole fraction of species i
z	Position from the inlet of the catalyst bed (m)

Greek letters

ε_b	Catalyst bed void fraction (porosity)
η_j	Effectiveness factor of reaction j
λ_z^f	Effective thermal conductivity (W K^{-1})
λ_g	Average gas thermal conductivity (W K^{-1})
λ_z^0	Axial thermal conductivity (W K^{-1})
λ_g	Solid thermal conductivity (W K^{-1})
μ_g	Gas dynamic viscosity (kg m^{-1} s^{-1})
ρ_g	Gas phase density (kg m^{-3})

ρ_{bed}	Density of the catalyst bed (kg m^{-3})
ΔH_{rxn}	Heat of reaction (J mol^{-1})
ΔS°	Entropy of reaction (J K^{-1})
ΔP	Pressure drop (Pa)
τ_{cat}	Catalyst tortuosity
τ	Dimensionless time
$\Sigma_i \nu_i$	Special atomic diffusion volumes
ζ	Dimensionless position from the inlet of the catalyst bed
ϕ	Thiele modulus

■ REFERENCES

(1) Rouwenhorst, K. H. R.; Engelmann, Y.; Van 'T Veer, K.; Postma, R. S.; Bogaerts, A.; Lefferts, L. Plasma-driven catalysis: Green ammonia synthesis with intermittent electricity,. *Green Chem.* **2020**, *22*, 6258−6287.

(2) Rouwenhorst, K. H. R.; Jardali, F.; Bogaerts, A.; Lefferts, L. From the Birkeland-Eyde process towards energy-efficient plasma-based NOx: synthesis: A techno-economic analysis,. *Energy Environ. Sci.* **2021**, *14*, 2520−2534.

(3) Fridman, A.*Plasma Chemistry*; Cambridge University Press: Cambridge, U.K., 2008; pp 4−5.

(4) Neyts, E. C.; Ostrikov, K.; Sunkara, M. K.; Bogaerts, A. Plasma Catalysis: Synergistic Effects at the Nanoscale,. *Chem. Rev.* **2015**, *115*, 13408−13446.

(5) Henis, J. M.Nitrogen oxide decomposition process, U.S. Patent 3983021, 1976.

(6) Rapakoulias, D.; Cavadias, S.; Amouroux, J. Processus catalytiques dans un réacteur à plasma hors d'équilibre II. Fixation de l'azote dans le système N2-O2,. *Rev. Phys. Appliquée* **1980**, *15*, 1261−1265.

(7) Mutel, B.; Dessaux, O.; Goudmand, P. Energy cost improvement of the nitrogen oxides synthesis in a low pressure plasma,. *Rev. Phys. Appliquée* **1984**, *19*, 461−464.

(8) Sun, Q.; Zhu, A.; Yang, X.; Niu, J.; Xu, Y. Formation of NOx from N2 and O2 in catalyst-pellet filled dielectric barrier discharges at atmospheric pressure,. *Chem. Commun.* **2003**, *3*, 1418−1419.

(9) Maltsev, A. N.; Belova, V. M.; Eremin, E. N. Heterogeneous catalytic oxidation of nitrogen in a glow discharge II 1:1 nitrogen-oxygen mixture. *Russ. J. Phys. Chem.* **1978**, *52*, 968−970.

(10) Maltsev, A. N.; Belova, V. M.; Eremin, E. N. Heterogeneous catalytic oxidation ofnitrogen in a glow discharge III. N2:O2 ∼ 1:4 nitrogen-oxygen mixture. *Russ. J. Phys. Chem.* **1978**, *52*, 970−972.

(11) Levenspiel, O. Chemical Reaction Engineering. *Ind. Eng. Chem. Res.* **1999**, *38*, 293−320.

(12) Abu Reesh, I. M. Acrylonitrile process enhancement through waste minimization: Effect of reaction conditions and degree of backmixing. *Sustainability* **2021**, *13*, 7923.

(13) Ma, H.; Sharma, R. K.; Welzel, S.; van de Sanden, M. C. M.; Tsampas, M. N.; Schneider, W. F. Observation and rationalization of nitrogen oxidation enabled only by coupled plasma and catalyst. *Nat. Commun.* **2022**, *13*, 1−10.

(14) Franco, D. S. P.; Fagundes, J. L. S.; Georgin, J.; Salau, N. P. G.; Dotto, G. L. A mass transfer study considering intraparticle diffusion and axial dispersion for fixed-bed adsorption of crystal violet on pecan pericarp (Carya illinoensis). *Chem. Eng. J.* **2020**, *397*, 125423.

(15) Sulaymon, A. H.; Ahmed, K. W. Competitive adsorption of furfural and phenolic compounds onto activated carbon in fixed bed column,. *Environ. Sci. Technol.* **2008**, *42*, 392−397.

(16) Reynolds, W.; Singer, H.; Schug, S.; Smirnova, I. Hydrothermal flow-through treatment of wheat-straw: Detailed characterization of fixed-bed properties and axial dispersion,. *Chem. Eng. J.* **2015**, *281*, 696−703.

(17) Aguilera, P. G.; Gutiérrez Ortiz, F. J. Prediction of fixed-bed breakthrough curves for H2S adsorption from biogas: Importance of axial dispersion for design,. *Chem. Eng. J.* **2016**, *289*, 93−98.

(18) Bittante, A.; García-Serna, J.; Biasi, P.; Sobrón, F.; Salmi, T. Residence time and axial dispersion of liquids in Trickle Bed Reactors at laboratory scale,. *Chem. Eng. J.* **2014**, *250*, 99−111.

(19) Ferreira, M. V.; Ribeiro, A. M.; Loureiro, J. M. Experimental and simulation studies of TAME synthesis in a fixed-bed reactor,. *Ind. Eng. Chem. Res.* **2007**, *46*, 1105−1113.

(20) Voggenreiter, J.; Ferre, A.; Burger, J. Scale-up of the Continuous Production of Poly(oxymethylene) Dimethyl Ethers from Methanol and Formaldehyde in Tubular Reactors,. *Ind. Eng. Chem. res.* **2022**, *61*, 10034−10046.

(21) Abbas, S. Z.; Dupont, V.; Mahmud, T. Kinetics study and modelling of steam methane reforming process over a NiO/Al2O3 catalyst in an adiabatic packed bed reactor,. *Int. J. Hydrogen Energy* **2017**, *42*, 2889−2903.

(22) Maqbool, F.; Abbas, S. Z.; Ramirez-Solis, S.; Dupont, V.; Mahmud, T. Modelling of one-dimensional heterogeneous catalytic steam methane reforming over various catalysts in an adiabatic packed bed reactor,. *Int. J. Hydrogen Energy* **2021**, *46* (7), 5112−5130.

(23) Gultekin, S.; Kalbekov, A. Effect of backmixing on the performance of bubble column reactors,. *Int. J. Dev. Res.* **2017**, *7*, 2.

(24) Colli, A. N.; Bisang, J. M. Evaluation of the hydrodynamic behaviour of turbulence promoters in parallel plate electrochemical reactors by means of the dispersion model,. *Electrochim. Acta* **2011**, *56*, 7312−7318.

(25) Colli, A. N.; Bisang, J. M. Study of the influence of boundary conditions, non ideal stimulus and dynamics of sensors on the evaluation of residence time distributions,. *Electrochim. Acta* **2015**, *176*, 463−471.

(26) Levenspiel, O.; Bischoff, K. B. Patterns of Flow in Chemical Process Vessels,. *Adv. Chem. Eng.* **1964**, *4*, 95−198.

(27) Sabri, E. Fluid flow through packed columns. *Chem. Eng. Prog.* **1952**, *48*, 89−94.

(28) He, G. Performance Degradation and Recovery of YSZ Membrane under the Sulphuric Acid Thermal Decomposition. The University of Sheffield, 2013.

(29) Fang, P.; Wang, J.; Li, X.; Wu, S.; Zhang, W.; Li, S. Effect of platinum on sintering morphology of porous YSZ ceramics,. *Microsc. Res. Technol.* **2017**, *80*, 889−897.

(30) Falsig, H.; Shen, J.; Khan, T. S.; guo, W.; jones, G.; Dahl, S.; Bligaard, T. On the structure sensitivity of direct NO decomposition over low-index transition metal facets,. *Top. Catal.* **2014**, *57* (1−4), 80−88.

(31) Treanor, C. E.; Rich, J. W.; Rehm, R. G. Vibrational relaxation of anharmonic oscillators with exchange-dominated collisions. *J. Chem. Phys.* **1968**, *48*, 1798−1807.

(32) Ricard, A.; Sarrette, J. P.; Oh, S. G.; Kim, Y. K. Comparison of the Active Species in the RF and Microwave Flowing Discharges of N2 and Ar-20%N2,. *Plasma Chem. Plasma Process.* **2016**, *36*, 1559−1570.

(33) Mehta, P.; Barboun, P.; Herrera, F. A.; Kim, J.; Rumbach, P.; Go, D. B.; Hicks, J. C.; Schneider, W. F. Overcoming ammonia synthesis scaling relations with plasma-enabled catalysis,. *Nat. Catal.* **2018**, *1*, 269−275.

(34) Capitelli, A. M.; Ferreira, C.M.; Gordiets, B. F.*Plasma Kinetics in Atmospheric Gases*, 31st ed.; Springer-Verlag Berlin Heidelberg, 2000; Vol. *31*, p 168.

(35) Zeldovich, J. The oxidation of nitrogen in combustion and explosions,. *Eur. Phys. J. A. Hadron. Nucl.* **1946**, *21*, 577−628.

(36) Nahomy, J; Ferreira, C M; Gordiets, B; Pagnon, D; Touzeau, M; Vialle, M Experimental and theoretical investigation of a n2−02 dc flowing glow discharge,. *J. Phys. D. Appl. Phys.* **1995**, *28*, 738.

(37) Pintassilgo, C. D.; Loureiro, J.; Guerra, V. Modelling of a N2-O2 flowing afterglow for plasma sterilization,. *J. Phys. D. Appl. Phys.* **2005**, *38*, 417−430.

(38) Kutasi, K.; Pintassilgo, C. D.; Loureiro, J.; Coelho, P. J. Active species in a large volume N2-O2 post-discharge reactor,. *J. Phys. D. Appl. Phys.* **2007**, *40*, 1990−2001.

(39) De Benedictis, S.; Dilecce, G. Time resolved diagnostics for kinetic studies in N2/O2 pulsed rf discharges,. *J. Phys. III* **1996**, *6*, 1189−1204.

(40) Ricard, A.; Sarrette, J. P.; Jeon, B.; Kim, Y. K. Discharge source-dependent variation in the densities of active species in the flowing afterglows of N2 RF and UHF plasmas,. *Curr. Appl. Phys.* **2017**, *17*, 945−950.

(41) Kemaneci, E.; Booth, J. P.; Chabert, P.; Van Dijk, J.; Mussenbrock, T.; Brinkmann, R. P. A computational analysis of the vibrational levels of molecular oxygen in low-pressure stationary and transient radio-frequency oxygen plasma,. *Plasma Sources Sci. Technol.* **2016**, *25*, 025025.

(42) Vašina, P.; Kudrle, V.; Tálský, A.; Botoš, P.; Mrázková, M.; Meško, M. Simultaneous measurement of N and O densities in plasma afterglow by means of NO titration,. *Plasma Sources Sci. Technol.* **2004**, *13*, 668−674.

(43) Nemec, D.; Levec, J. Flow through packed bed reactors: 1. Single-phase flow,. *Chem. Eng. Sci.* **2005**, *60*, 6947−6957.

(44) Chandra, V.; Vogels, D.; Peters, E. A. J. F.; Kuipers, J. A. M. A multi-scale model for the Fischer-Tropsch synthesis in a wall-cooled packed bed reactor,. *Chem. Eng. J.* **2021**, *410*, 128245.

(45) Harode, H.; Ramteke, M. Axial dispersion modeling of industrial hydrocracking unit and its multiobjective optimization,. *Chem. Eng. Res. Des.* **2017**, *121*, 57−68.

(46) Palys, M. J.; McCormick, A.; Cussler, E. L.; Daoutidis, P. Modeling and optimal design of absorbent enhanced ammonia synthesis,. *Processes* **2018**, *6*, 91.